Electronic structure of the ternary pnictide semiconductors $ZnSiP_2$, $ZnGeP_2$, $ZnSnP_2$, $ZnSiAs_2$, and $MgSiP_2$

J. E. Jaffe* and Alex Zunger
Solar Energy Research Institute, Golden, Colorado 80401
(Received 5 March 1984)

Self-consistent all-electron density-functional electronic-structure calculations are reported for five II-IV-V_2 chalcopyrite-structure semiconductors. Chemical trends in the band structure, bonding, and charge distribution are identified. The role of the zinc $3d$ orbitals is clarified. We also discuss the effect of the structural distortion relative to the zinc-blende analogs on the bonding and principal band gaps.

I. INTRODUCTION

Ternary ABC_2 semiconductors having the chalcopyrite structure[1,2] show considerable promise for a range of technological applications, including solar cells[3] and infrared parametric oscillators.[4] Research on these materials has been mostly experimental,[1,2] but there have also been a number of band-structure calculations for compounds in this group.[5–24] A limitation of most of these theoretical studies[5–21] has been the use of the empirical pseudopotential method (EPM), where (i) the cation (Zn, Cd, or Cu) d orbitals are neglected, (ii) the electronic charge density and the attendant screening are described non-self-consistently, and (iii) it is assumed that the potential form factors that pertain to binary zinc-blende compounds (where each anion is coordinated by four identical cations) are also applicable to the ternary ABC_2 system (where each anion C is coordinated by two A-type cations and two B-type cations). At the same time, the advantage of the EPM approach lies in its flexibility to emulate the experimentally known optical gaps into the band-structure calculation through small adjustments of the parameters, usually producing a perfect agreement with the available data.

The present authors have previously described a series of all-electron, nonempirical self-consistent studies of the electronic structure of I-III-VI_2 chalcopyrites[23] (e.g., $CuInSe_2$) where the presence of chemically active Cu $3d$ orbitals at the vicinity of the top of the valence band makes the EPM particularly problematic. In the present paper we extend these calculations to five of the II-IV-V_2 chalcopyrite-structure ternary pnictides. While existing EMP calculations for many of these compounds are adequate and generally produce fundamental band gaps in

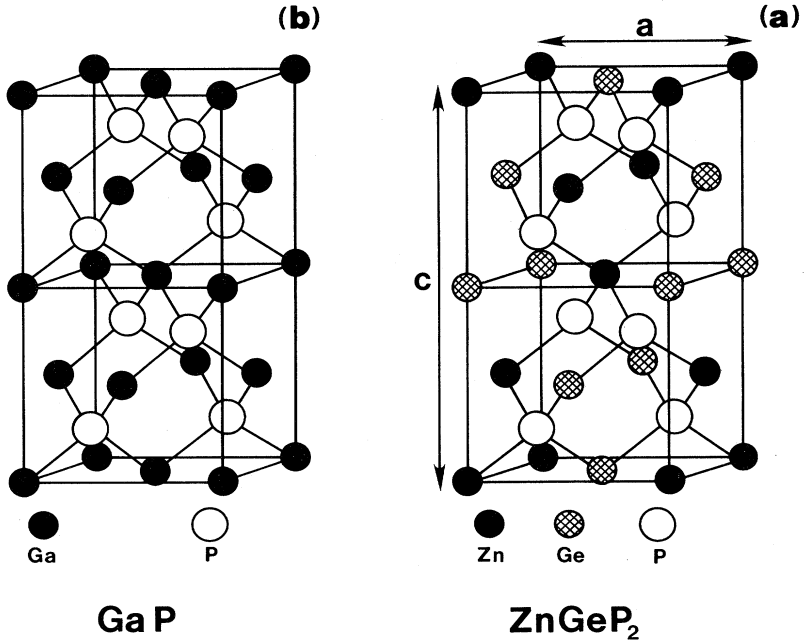

FIG. 1. Comparison of the crystal structure of a binary zinc-blende semiconductor (GaP) with that of a ternary pnictide ($ZnGeP_2$), having the chalcopyrite structure.

good agreement with the available experimental data, the present calculations are intended to answer some questions about these compounds, such as covalency versus ionicity and the role of Zn d orbitals, that the EPM does not treat well.

The II-IV-V_2 ternary pnictides ($A^{(II)}B^{(IV)}C_2^{(V)}$) can be thought of as ternary analogs of the binary III-V zinc-blende semiconductors.[23,24] There are three notable differences: (i) replacement of half of the atoms of the column-III element by those of column-IIA (Mg) or -IIB (Zn, Cd) element, and the other half by those of column-IV (Si, Ge, or Sn) element in an *ordered* fashion, leading to the double crystallographic unit cell shown in Fig. 1, (the *primitive* unit cell being now 4 times larger); (ii) a slight tetragonal compression (except in $ZnSnC_2^{(V)}$ compounds) along the c axis, leading to nonideal tetragonal distortion parameters $\eta \equiv c/2a \neq 1$; and (iii) a distortion of the anion sublattice involving a shift by each anion away from its nearest neighbors of one cation and towards those of the other kind of cation. This leads to a nonideal anion displacement parameter $u \neq \frac{1}{4}$. The present authors have shown[24–26] that the anion shift is primarily a consequence of atomic sizes (tetrahedral covalent radii) in that if the column-II atom is larger than the column-IV atom, then each $A^{(II)}$–$C^{(V)}$ bond is lengthened and each $B^{(IV)}$–$C^{(V)}$ bond is shortened relative to an ideal zinc-blende structure with the ternary compound's lattice constant. This is the case in all known II-IV-V_2 materials—except the $ZnSnC_2^{(V)}$ systems, where the situation is reversed—the Sn–$C^{(V)}$ bond is longer than the Zn–$C^{(V)}$ bond. The anion sublattice distortion and tetragonal compression are related, for most of these compounds, in such a way as to maintain (almost) perfectly tetrahedral bond angles at the column-IV atom.[24] Again, the three $ZnSnC_2^{(V)}$ compounds are the exception, since they have $\eta \equiv c/2a \equiv 1$ (while tetrahedrality around the Sn site would require $\eta \simeq 1.03$). As a consequence of these structural differences from the III-V compounds, we find characteristic differences in the electronic properties of the II-IV-V_2 group, as will be described below.

II. BAND-STRUCTURE CALCULATIONS

We calculate the electronic structure of five II-IV-V_2 compounds using the local-density potential-variation

TABLE I. Experimental values of the cubic lattice constant a, tetragonal distortion parameter $\eta \equiv c/2a$, and anion displacement parameter u used in the present calculation.

Compound	a (a.u.)	η	u
$ZnSiP_2$	10.20264	0.96638	0.2691[a]
$ZnGeP_2$	10.31791	0.9800	0.25816[b]
$ZnSnP_2$	10.67885	1.0000	0.239[c]
$ZbSiAs_2$	10.58247	0.9700	0.26565[b]
$MgSiP_2$	10.81113	0.8823	0.292[d]

[a]Reference 30.
[b]Reference 31.
[c]Reference 32.
[d]Reference 33.

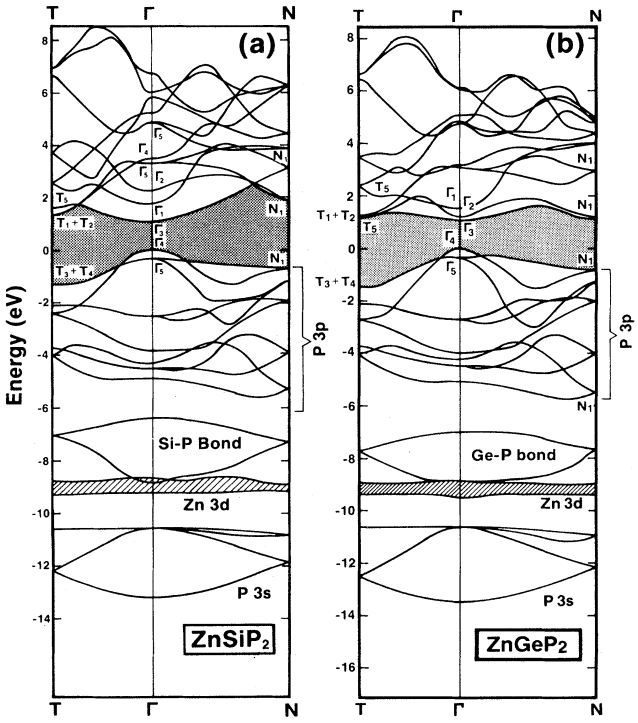

FIG. 2. Self-consistent band structure of (a) $ZnSiP_2$ and (b) $ZnGeP_2$ using the Ceperley-Alder exchange-correlation potential. Crystal-structure parameters are given in Table I.

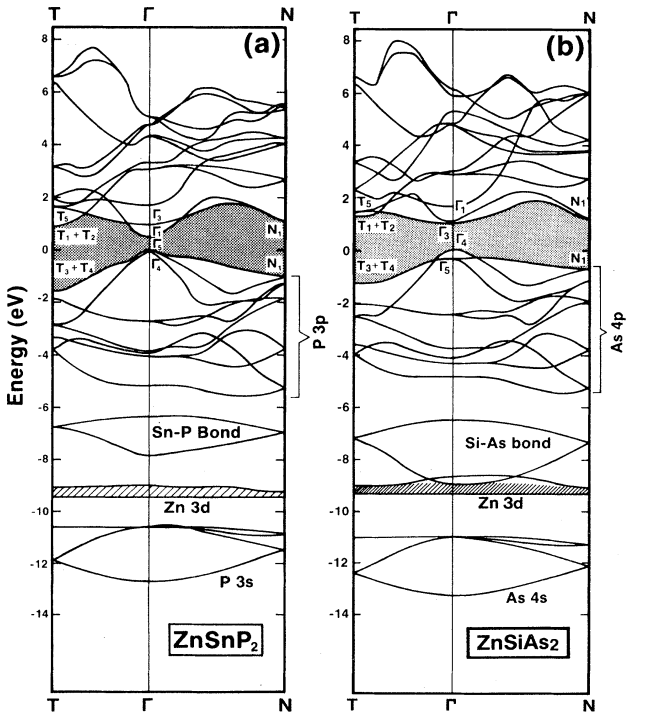

FIG. 3. Self-consistent band structure of (a) $ZnSnP_2$ and (b) $ZnSiAs_2$ using the Ceperley-Alder exchange-correlation potential. Crystal-structure parameters are given in Table I.

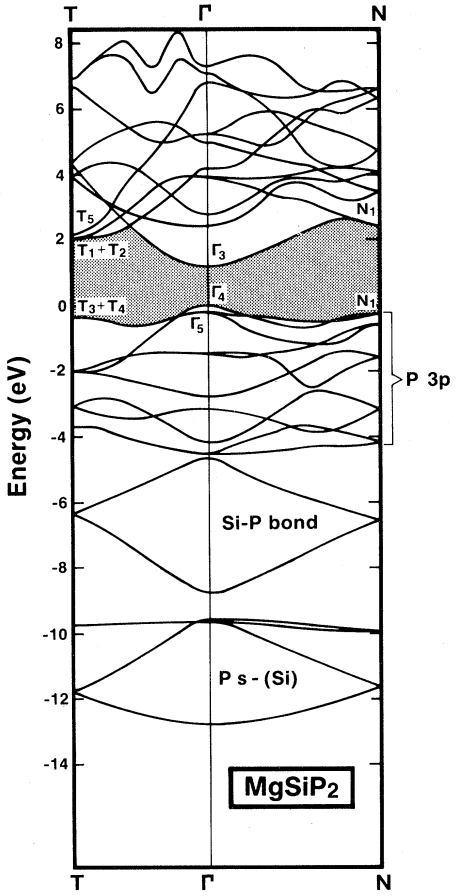

FIG. 4. Self-consistent band structure of $MgSiP_2$ using the Ceperley-Alder exchange-correlation. Crystal-structure parameters are given in Table I.

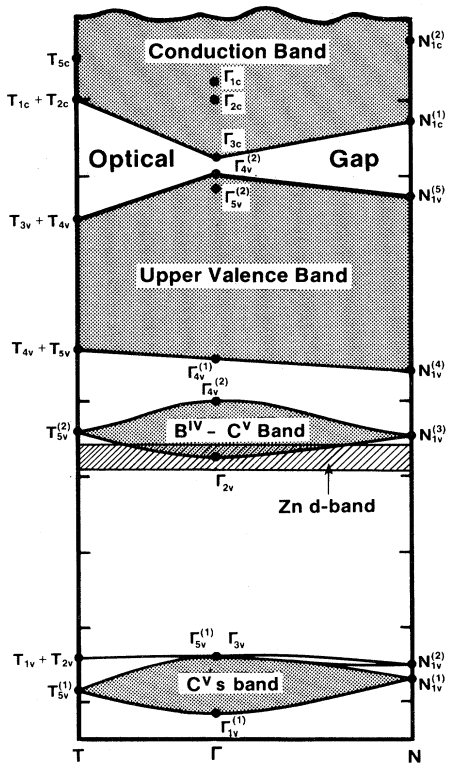

FIG. 5. Generic band-structure diagram of a II-IV-V_2 ternary pnictide.

mixed-basis (PVMB) approach, which has been described in detail elsewhere.[23,27] We have employed the Ceperley-Alder[28] form of the exchange-correlation function. The PVMB is an *ab initio* method: no experimental data, except for the crystal structure of the compound in question, are used as input; there are no pseudopotentials or shape approximations (e.g., muffin tin) involved; and the charge density in the unit cell is recalculated iteratively until a high degree of self-consistency is obtained. Special techniques are used to obtain efficient convergence to self-consistency[27] and to diagonalize the large ($\sim 500\times 500$) Hamiltonian matrices[29] without having to store them (except one row at a time). After reaching self-consistency, bands are calculated on a coarse mesh of points along two high-symmetry lines ($T\rightarrow\Gamma\rightarrow N$) in the Brillouin zone. Band connectivities are worked out by examining overlap integrals between wave functions for different bands at successive $\vec{k}$ points. The values of the crystal-structure parameters used in the band-structure calculation are given in Table I.[30–33] Values of a, u, and η were taken from experiment,[30–33] with the following exceptions: For $ZnSiP_2$ we performed calculations with the experimental value $u=0.269$, and the zinc-blende-like value $u=0.250$, while for $MgSiP_2$ we used two predicted values, namely $u=0.2848$ from the model[24] of conservation of tetrahedral bond lengths, and $u=0.3134$ from the model[24] of the simple tetrahedral rule, using $\eta=\eta_{\text{expt}}$, which turned out to bracket the measured value[33] $u=0.292$. These multiple values for u permits us to study the influence of this anion displacement parameter on the electronic structure.

III. BAND STRUCTURE

The electronic band structures of $ZnSiP_2$ and $ZnGeP_2$ are displayed in Figs. 2(a) and 2(b); those of $ZnSnP_2$ and $ZnSiAs_2$ are displayed in Figs. 3(a) and 3(b); the band structure of $MgSiP_2$ is given in Fig. 4. Because of the complexity of these bands, in Fig. 5 we give a schematic view of a generic band structure of the $ZnSiP_2$-type materials, establishing the main subbands and the band notations to be used below. Table II gives the energies of the high-symmetry states, as denoted in Fig. 5, relative to the valence-band maximum (VBM).

There are four main valence subbands in the region between E_{VBM} and $E_{\text{VBM}}-14$ eV (cf. Fig. 5). First, the upper valence band extends from E_{VBM} to about $E_{\text{VBM}}-5$ eV and is constructed predominantly from the (column-V) anion p states, admixed with the column-II-atom sp states and column-IV-atom p states. This band is separated by a heteropolar gap from the second valence band that lies below it: The $B^{(\text{IV})}$–$C^{(\text{V})}$ bonding band, representing strong overlaps of the Si,Ge,Sn orbitals with

TABLE II. Calculated valence-band energies (in eV) at high-symmetry points, given relative to $\Gamma_{4v}^{(2)}$ [the valence-band (VB) maximum, except in $ZnSnP_2$]. For notation, refer to Fig. 5. The Ceperley correlation was used, together with the crystal-structure parameters of Table I (but $u=0.3134$ for $MgSiP_2$).

State \ Compound	$ZnSiP_2$	$ZnGeP_2$	$ZnSnP_2$	$ZnSiAs_2$	$MgSiP_2$
Upper VB:					
Maxima					
$\Gamma_{4v}^{(2)}$	0.00	0.00	0.00	0.00	0.00
$\Gamma_{5v}^{(2)}=\Delta_{CF}$	−0.30	−0.33	+0.012	−0.32	−0.22
$T_{3v}+T_{4v}$	−1.25	−1.50	−1.52	−1.26	−0.38
$N_{1v}^{(5)}$	−0.67	−0.86	−1.00	−0.69	−0.31
Minima					
$\Gamma_{4v}^{(1)}$	−4.84	−5.10	−5.18	−4.81	−4.53
$T_{4v}+T_{5v}$	−3.94	−4.09	−3.77	−3.97	−3.69
$N_{1v}^{(4)}$	−5.28	−5.51	−5.24	−5.25	−4.19
$B^{(IV)}$-$C^{(V)}$ band:					
$\Gamma_{4v}^{(2)}$	−6.37	−7.02	−6.32	−6.48	−4.67
$\Gamma_{2v}^{(2)}$	−8.79	−8.89	−7.74	−8.75	−8.76
$T_{5v}^{(2)}$	−7.00	−7.73	−6.70	−7.17	−6.36
$N_{1v}^{(3)}$	−7.25	−7.87	−6.93	−7.35	−6.55
Zn $3d$ bands:					
Maximum at Γ	−8.61	−8.86	−9.01	−8.92	
Minimum at Γ	−9.20	−9.52	−9.47	−9.29	
Maximum at T	−8.78	−9.08	−9.06	−9.01	
Minimum at T	−9.24	−9.35	−9.44	−9.30	
Maximum at N	−8.90	−9.10	−9.24	−9.07	
Minimum at N	−9.15	−9.34	−9.46	−9.26	
$C^{(V)}$ s bands:					
$\Gamma_{5v}^{(1)}$	−10.53	−10.62	−10.64	−11.03	−9.66
Γ_{3v}	−10.53	−10.64	−10.58	−11.01	−9.59
$\Gamma_{1v}^{(1)}$	−13.15	−13.46	−12.67	−13.26	−12.78
$T_{1v}+T_{2v}$	−10.54	−10.65	−10.61	−11.04	−9.75
$T_{5N}^{(1)}$	−12.18	−12.50	−11.58	−12.40	−11.80
$N_{1v}^{(2)}$	−10.81	−10.96	−10.87	−11.30	−9.94
$N_{1v}^{(1)}$	−11.84	−12.18	−11.49	−12.11	−11.64

the P or As orbitals. The third band is the Zn $3d$ state which is relatively narrow, and either intersects the $B^{(IV)}-C^{(V)}$ band (in $ZnGeP_2$, $ZnSiAs_2$, and $ZnSiP_2$), or appears just below it (in $ZnSnP_2$). The closeness of the Zn d band to the $B^{(IV)}-C^{(V)}$ bonding valence band highlights the difficulty in the empirical pseudopotential calculations that omit this band altogether, while retaining the band below it. The latter (fourth) subband is an anion s band; when it is near the $B^{(IV)}-C^{(V)}$ subband (e.g., in $MgSiP_2$) it hybridizes with the $B^{(IV)}$ orbitals.

TABLE III. Comparison of observed (Ref. 16) x-ray photoelectron spectroscopy (XPS) and calculated positions of structures in the density of states of $ZnGeP_2$ compounds. Results are given relative to the $\Gamma_{4v}^{(2)}$ state; Al $K\alpha$ x rays were used in the XPS measurements (Ref. 16). All energies are given in eV.

Feature	$ZnGeP_2$ Expt.	$ZnGeP_2$ Calc.
Position of maximum in upper VB	2.3	2.1
Bottom of upper VB	5.5	5.5
Ge–P bond	7.0	7.8
Center of Zn $3d$	9.7	9.2
P $3s$ band center	12.5	11.5

The top of the upper valence band at Γ consists of two components, Γ_{5v} and Γ_{4v}, split by the crystal-field (CF) energy $\Delta_{CF}\equiv\epsilon(\Gamma_{5v})-\epsilon(\Gamma_{4v})$. The crystal-field pair is inverted ($\Delta_{CF}<0$) in all components shown but $ZnSnP_2$. The width of the upper valence band at Γ increases progressively with increasing atomic number of the $B^{(IV)}$ atom (compare the series $ZnSiP_2$, $ZnGeP_2$, and $ZnSnP_2$). On the other hand, the width of the $B^{(IV)}-C^{(V)}$ band at Γ decreases with increasing atomic number of the $B^{(IV)}$ atom (2.4, 1.7, and 1.4 eV for $ZnB^{(IV)}P_2$, with $B^{(IV)}$=Si,

TABLE IV. Calculated and measured lowest direct and pseudodirect band gaps and crystal-field splittings (in eV) of five ternary pnictides. We have $E_g(\text{pseudo})=\Gamma_{3v}-\Gamma_{4v}$, $E_g(\text{direct})=\Gamma_{1c}-\Gamma_{4v}$, and $\Delta_{CF}=\Gamma_{5v}-\Gamma_{4v}$. We use $u=u_{\text{expt}}$ (Table I), except for $MgSiP_2$ ($u=0.3134$).

Gap	$ZnSiP_2$	$ZnGeP_2$	$ZnSnP_2$	$ZnSiAs_2$	$MgSiP_2$
E_g^{calc}(pseudo)	1.11	1.09	0.97	0.96	1.16
E_g^{expt}(pseudo)	2.07	1.99		1.74	2.2
E_g^{calc}(direct)	1.81	1.19	0.61	1.01	2.40
E_g^{expt}(direct)	2.96	2.34	1.66	2.12	
Δ_{CF}(calc)	−0.30	−0.33	+0.012	−0.32	−0.22
Δ_{CF}(expt)	−0.13	−0.08	0.000	−0.13	

TABLE V. Our results for the internal structure of the conduction bands, described by giving the conduction-band states relative to the conduction-band minima (Γ_{1c} in $ZnSnP_2$, Γ_{3c} in all others) in eV.

State	$ZnSiP_2$	$ZnGeP_2$	$ZnSnP_2$	$ZnSiAs_2$	$MgSiP_2$
Γ_{3c}	0.00	0.00	0.36	0.00	0.00
Γ_{1c}	0.70	0.10	0.00	0.05	1.24
Γ_{2c}	1.26	0.44	1.10	0.70	1.60
$T_{1c}+T_{2c}$	0.29	0.14	0.29	0.27	0.86
T_{5c}	0.56	0.11	1.01	0.43	0.96
$N_{1c}^{(1)}$	0.80	0.04	0.51	0.19	1.24
$N_{1c}^{(2)}$	2.04	1.86	2.06	1.71	2.24

TABLE VI. Comparison of the present nonempirical, all-electron self-consistent band structures of $ZnGeP_2$ and $ZnSiAs_2$ at Γ with a number of empirical pseudopotential calculations. Results are given in eV relative to the valence-band maximum.

	$ZnGeP_2$ ($u=0.2582$)			$ZnSiAs_2$ ($u=0.2657$)		
State	Present all electron	Ref. 19 EPM	Ref. 15 EPM	Present all electron	Ref. 19 EPM	Ref. 19 EPM
Upper VB						
$\Gamma_{4v}^{(2)}$	0.00	0.00	0.00	0.00	0.00	0.00
$\Delta_{CF}=\Gamma_{5v}^{(2)}$	−0.33	−0.003	+0.03	−0.32	−0.04	−0.07
$\Gamma_{4v}^{(1)}$	−5.10	−3.86	−3.38	−4.81	−3.62	
$B^{(\text{IV})}$–$C^{(\text{V})}$ bond						
$\Gamma_{4v}^{(2)}$	−7.02	−5.78	−6.24	−6.48	−5.04	
$\Gamma_{2v}^{(2)}$	−8.89	−8.80	−7.72	−8.75	−8.16	
$C^{(\text{V})}$ s band						
$\Gamma_{5v}^{(1)}$	−10.62	−10.94	−10.68	−11.03	−10.67	
Γ_{3v}	−10.64	−11.05	−10.59	−11.01	−10.75	
$\Gamma_{1v}^{(1)}$	−13.46	−13.54	−13.04	−13.26	−13.01	
Zn $3d$ band, Γ	−9.19			−9.11		
Conduction band						
Γ_{1c}	1.19	2.29	2.31	1.01	2.21	2.17
Γ_{3c}	1.09	1.96	2.60	0.96	1.81	2.11
Γ_{2c}	1.53	2.73	2.70	1.66	2.91	3.56
$\Gamma_{5c}^{(1)}$	3.08	4.49	4.98	2.88	4.62	
Γ_{4c}	3.16	4.80	5.07	2.98	4.82	
$\Gamma_{5c}^{(2)}$	4.76		6.26	4.81		

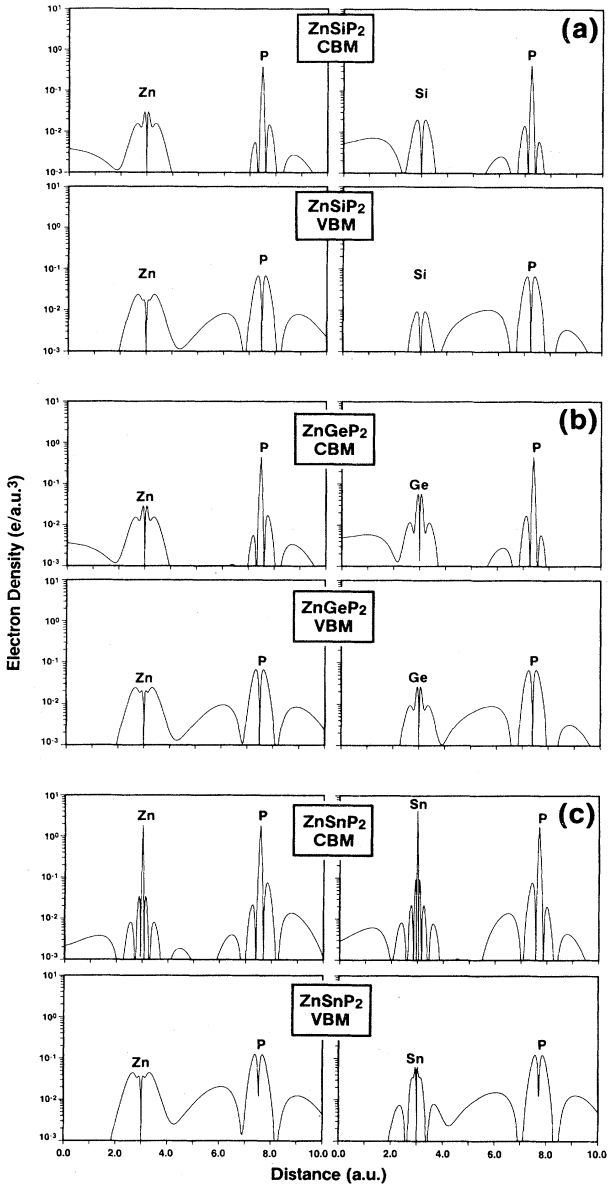

FIG. 6. Electronic charge density along the $A^{(II)}$–$C^{(V)}$ and $B^{(IV)}$–$C^{(V)}$ bonds at the top of the valence band (VBM) and bottom of the conduction band (CBM) for (a) $ZnSiP_2$, (b) $ZnGeP_2$, and (c) $ZnSnP_2$.

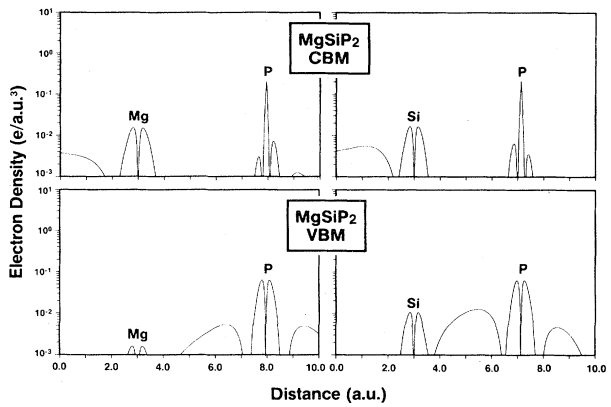

FIG. 7. Electronic charge density along the Mg–P and Si–P bonds at the top of the valence band (VBM) and bottom of the conduction band (CBM) in $MgSiP_2$.

Ge, and Sn, respectively), reflecting an increase in the $B^{(IV)}$–$C^{(V)}$ bond length and reduced interaction along this series. This tendency also reflects the near resonance of the isolated Si and P orbital energies, and the progressive departure from this close matching as one goes to $B^{(IV)}$=Ge, and finally to $B^{(IV)}$=Sn with its deep and nearly chemically inert s orbitals. $MgSiP_2$ is different from the Zn-based pnictides, in that its Si-P band is very wide, repelling upwards the top valence band and interacting with the anion band below it, to render to it some Si character. The significant difference between the electronic structure of the ternary ABC_2 chalcopyrites[23] (e.g., $CuInSe_2$) and ternary ABC_2 pnictides (e.g., $ZnSiP_2$) is that the transition-atom $3d$ band occurs in the former compounds inside the upper valence band (at about $E_{VBM}-3$ eV), affecting the optical properties at threshold,[23] whereas in the latter case the transition-atom $3d$ band occurs near the $B^{(IV)}$–$V^{(V)}$ band (at about $E_{VBM}-9$ eV), affecting primarily the $B^{(IV)}$–$C^{(V)}$ bond, with a much smaller compressing effect on the band gap.

Table III provides a comparison between the calculated peak positions of various features in the density of states and the experimental photoemission[16] data for $ZnGeP_2$. The agreement is generally very good. The experimental spectrum shows the separation of the upper valence band from the $B^{(IV)}$–$C^{(V)}$ band below it as a minimum at $E_{VBM}-6.2$ eV. The shoulder at deeper binding energies, around $E_{VBM}-7$ eV to $E_{VBM}-8$ eV corresponds to the $B^{(IV)}$–$C^{(V)}$ band. The Zn $3d$ peak overlaps with the bottom of this band, as is evident in the calculation [Fig. 2(b)]. In the EPM calculation,[16] the same spectral region was analyzed in terms of the $B^{(IV)}$–$C^{(V)}$ band alone, omitting Zn contributions. The observed[16] total valence-band width of (14.5±0.5) eV agrees reasonably well with our calculated value of 13.46 eV; we believe, however, that the experimental value is a bit too high as it was based on the identification of the shoulder at ~12.5 eV with a similar feature in the EMP calculation.[16] Our calculation does not support this conclusion from the EPM calculation (the EPM results are reasonable for the upper valence band, but less reliable at higher binding energies where the local pseudopotential approximation employed breaks down).

In constrast to the physically reasonable description of the valence-band states, the local-density-functional formulation of exchange and correlation is known[34] to severely underestimate valence- to conduction-band gaps. The extent of this underestimation is evident from Table IV that compares the calculated and measured lowest direct and indirect gaps in these systems. However, we notice that the *relative* positions of the calculated valence bands (i.e., the internal structure of all the valence bands taken as a group) is in fairly good agreement with experiment.[1] We obtain the correct signs for the crystal-field

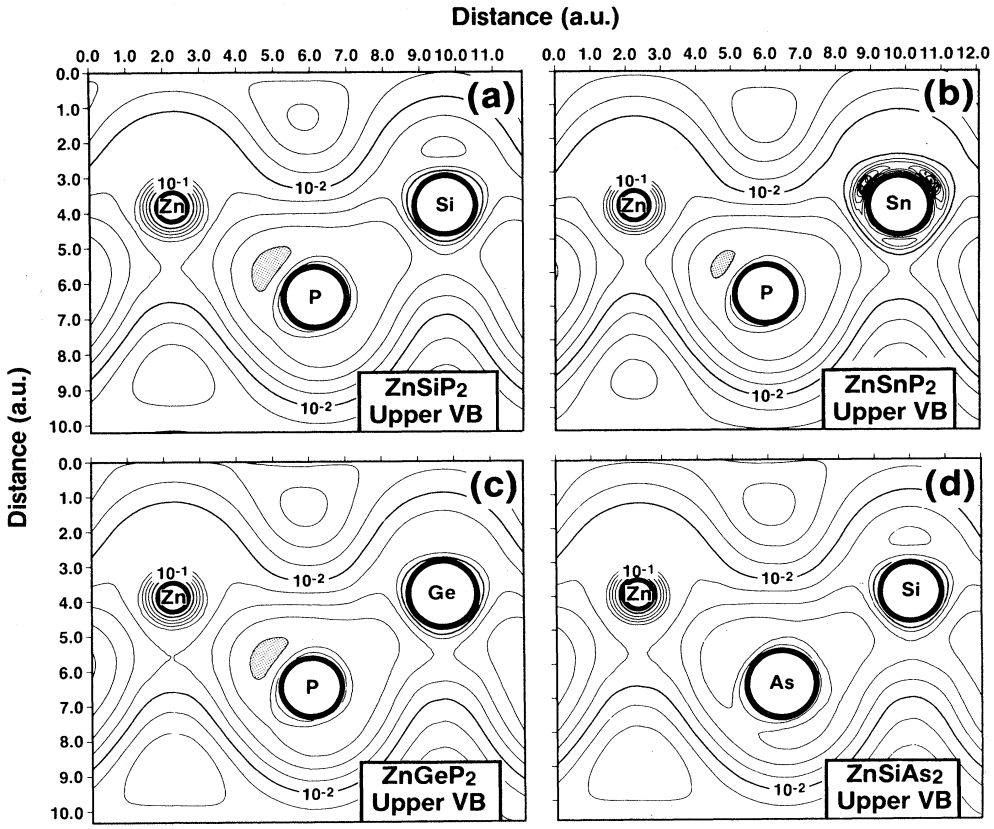

FIG. 8. Calculated electronic charge density in the upper valence band (cf. Fig. 5) of ternary pnictides. The contours are logarithmically spaced. Solid circles denote the core region, where the rapidly varying charge density was omitted for clarity of display. (a) $ZnSiP_2$, (b) $ZnSnP_2$, (c) $ZnGeP_2$, and (d) $ZnSiAs_2$. The shaded area highlights the peaked $A^{(II)}$–$C^{(V)}$ covalent-bond charge.

splittings Δ_{CF} (unlike the EPM calculation of Refs. 14–16), but the absolute magnitudes are consistently too large.

The general chemical trends of the gaps are closely reproduced, e.g., overall decrease with molecular weight, smaller for arsenides than for the comparable phosphides, larger for the A =Mg compound than for the comparable A =Zn compound. To compenstate partially for the systematic downshift of the conduction band underlying the density-functional approach, in Table V we show the conduction-band structure relative to the conduction-band minimum. The trends agree with experiment[1] in that we correctly predict the compounds with a pseudodirect gap[35] ($ZnSiP_2$, $ZnGeP_2$, and $ZnSiAs_2$). The nature of the lowest gap in $MgSiP_2$ is still not clear experimentally; hence the results of Table V constitute predictions. Note that in $ZnSiP_2$ we find states away from Γ (such as $T_{1c}+T_{2c}$) that have substantially lower energy than Γ_{1c}. These may be the final states of transitions at energies between the pseudodirect lowest gap $\Gamma_{4v}+\Gamma_{3c}$ and the onset of strong direct transitions $\Gamma_{4v}\rightarrow\Gamma_{1c}$. Such transitions away from Γ may be the source of some puzzling structure[36] found in the optical spectrum of $ZnSiP_2$.

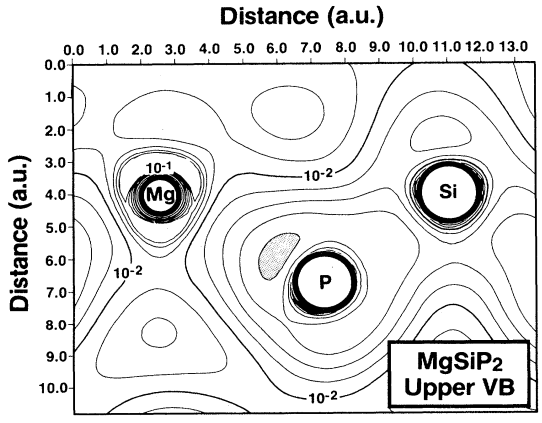

FIG. 9. Calculated electronic charge density in the upper valence band of $MgSiP_2$. The contours are logarithmically spaced. The solid circles indicate the core regions. The shaded area highlights the peaked ionic charge along the Mg–P bond near the P site.

It is interesting to consider the nature of the wave functions involved at the optical transition at threshold, i.e., at the top of the valence band and at the bottom of the conduction band along a chemical series of ternary pnictides (Fig. 6). Whereas the conduction-band minimum (CBM) has the traditionally accepted metal s character, it is obvious from Fig. 6 that as one progresses from $ZnSiP_2$ to $ZnGeP_2$ and $ZnSnP_2$, a significant anion character is built into the CBM wave function along the $B^{(IV)}$–$C^{(V)}$ bond.

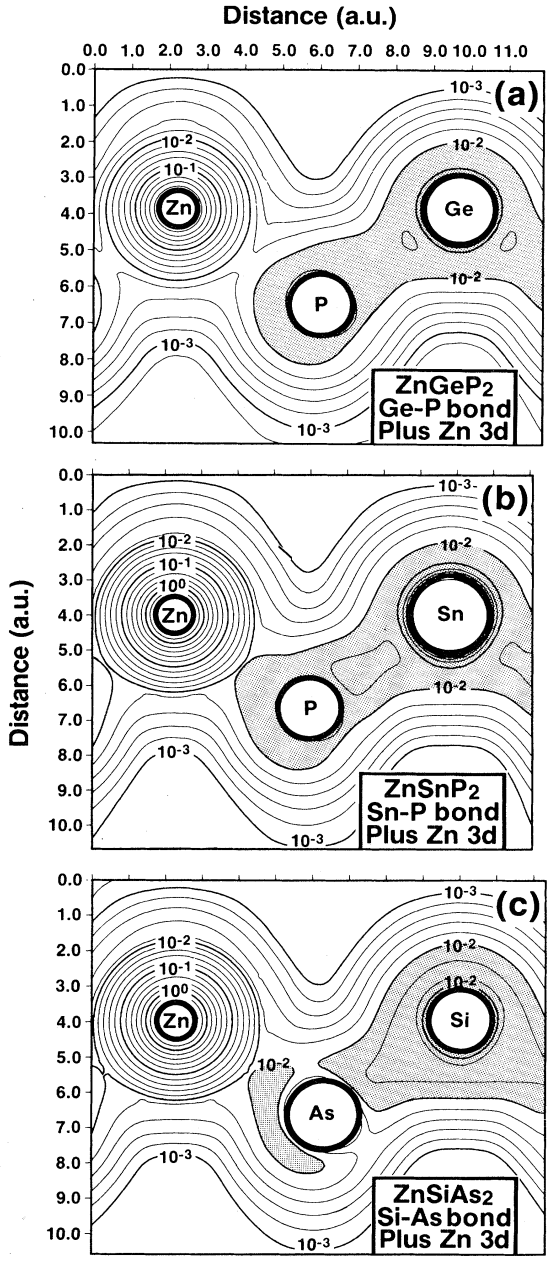

FIG. 10. Calculated electronic charge density corresponding to the $B^{(IV)}$-$C^{(V)}$ band and the Zn $3d$ band near it. The contours are logarithmically spaced. The solid circles indicate the core regions. The 10^{-2}-e/a.u.^{3} contours around the $C^{(V)}$ and $B^{(IV)}$ atoms are shaded to highlight the formation of the bonding $B^{(IV)}$-$C^{(V)}$ contact. Notice that the nearly spherical Zn $3d$ charge approaches the $A^{(II)}$—$C^{(V)}$ bond center, inhibiting the states from the $B^{(IV)}$-C$^{(V)}$ band from spilling over to the $A^{(II)}$ site.

This component is absent in the more ionic systems $MgSiP_2$ (Fig. 7). Indeed, the delineation into a nearly pure cation conduction-band wave function exists only in highly ionic materials (e.g., NaCl), where no atomic excited orbitals exist at the vicinity of the lowest cation valence s orbital. However, as one moves to less ionic systems

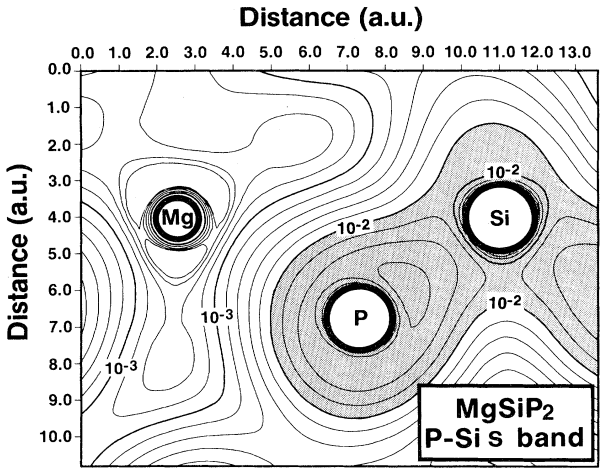

FIG. 11. Calculated electronic charge density corresponding to the P-Si band in $MgSiP_2$. The contours are logarithmically spaced. The solid circles indicate the core regions. The 10^{-2}-e/a.u.^{3} contours around P and Si are shaded to highlight the strong Si—P covalent bond formed in this energy region.

where excited anion orbitals exist near the characteristic energy of the metal s orbital, an hybrid conduction band is possible. This implies that in the covalent end of the pnictide series depicted in Fig. 6, the optical transition from the VBM to the CBM carries the system partially from an initial state on the anion sublattice to a final state on the metal sublattice (as in ionic systems), but, in part, this transition also involves a single-center component where both initial and final wave-function amplitudes reside on the anion sublattice, contributing significantly to the oscillator strength.

In Table VI we compare the results of the present self-consistent all-electron calculation for $ZnGeP_2$ and $ZnSiAs_2$ with empirical pseudopotential calculations.[9,15,19] In the calculations of de Alvarez *et al.*[15] and Polygalov *et al.*[9] the potential form factors $V_{Zn}(\vec{G})+V_{Ge}(\vec{G})$ are replaced by the form factor of the Ga-atom $V_{Ga}(\vec{G})$ obtained by fitting the bands of GaP and interpolating to the unit-cell volume of $ZnGeP_2$. Inherent in this virtual-crystal approximation is the assumption of the same screening in both crystals, the neglect of p-d and s-d hybridization with the Zn d states, and that the scattering from a P potential, when surrounded by four equal cations (as in GaP), is similar to the scattering from a P potential when surrounded by two different cations (two Zn and two Ge atoms in $ZnSiP_2$). The band Hamiltonian is diagonalized within a small basis of plane waves (69—84 waves, with an additional 244 waves added to lowest order in the perturbation). In the work of Heinrich *et al.*[19] the Zn form factors are taken as an average from ZnS and ZnSe, and those of P are taken from GaP. According to these authors, the freedom left in taking the form factors from different, equally reasonable, compounds results in variation of $\lesssim 0.25$ eV in the band energies, whereas far higher variations in the band structure (~ 1 eV), including the reversal of direct with indirect band gaps, are obtained if one uses form factors optimized for binary compounds without adjusting them to give

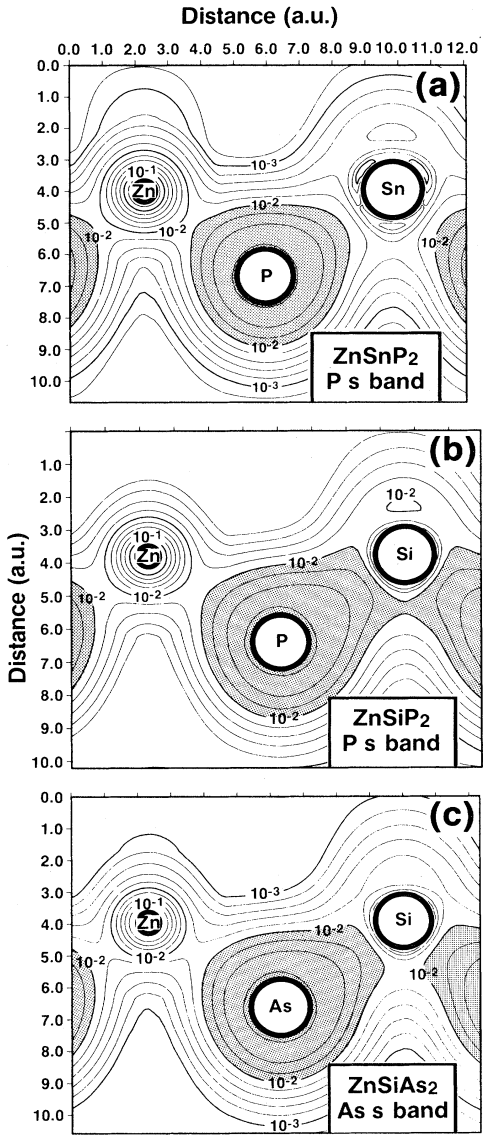

FIG. 12. Calculated electronic charge density of the $C^{(V)}$ s band (cf. Fig. 5). The contours are logarithmically spaced. The solid circles indicate the core regions. The 10^{-2}-e/a.u.^{3} contours around the anion are shaded to highlight the anion s character of this band. (a) $ZnSnP_2$, (b) $ZnSiP_2$, and (c) $ZnSiAs_2$. Notice that the asphericity around the anion decreases when the $B^{(IV)}$ atom is Sn, indicating a move towards a more isotropic (metallic) structure.

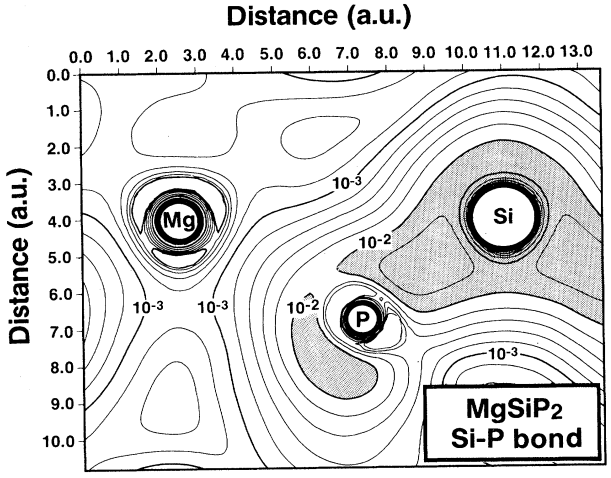

FIG. 13. Calculated electronic charge density of the Si-P band of $MgSiP_2$. The contours are logarithmically spaced. The solid circles indicate the core regions. The 10^{-2}-e/a.u.^{3} contours around P and Si are shaded to highlight the strong P—Si bond. Notice that unlike the Zn-based pnictides (Fig. 12), this band in $MgSiP_2$ shows a strong interaction with the Si site, and extends well into the domain of the $A^{(II)}$ site (as no d states are available on this site to repel the density away from it).

physically reasonable results. In all of the EPM calculations the crystal potential is described as a linear superposition of atom-centered spherical potentials. Table VI and the comparison of the various dispersion relations in Refs. 9, 15, and 19 with our Fig. 2(b) show that the EPM and the present result agree closely in the upper $\sim$4 eV below the top of the valence band. However, since hybridization with the Zn $3d$ states is not present in the EPM calculations, the bottom of the upper valence band ($\Gamma_{4v}^{(1)}$) and the top of the $B^{(IV)}$—$C^{(V)}$ band ($\Gamma_{4v}^{(2)}$) are both 1—1.5 eV too high. In the work of Alverez *et al.*[15] the underestimation of the width of the upper valence band is attributed to the use of a local pseudopotential in their calculations (i.e., Zn d and Zn sp orbitals experience the same, sp-like potential). The discrepancy with the present all-electron calculation is similar to the discrepancies between different fitting schemes in EPM calculations (differences of 1.1 eV for $\Gamma_{2v}^{(2)}$ and 0.5 eV for $\Gamma_{4v}^{(2)}$ between the EPM results of Refs. 19 and 15 for $ZnGeP_2$, whereas the difference between the present calculation and the average of the two EPM results is 1.0 and 0.6 eV for $\Gamma_{4v}^{(2)}$ and $\Gamma_{2v}^{(2)}$, respectively). As indicated before, while the EPM calculation correctly obtains large band gaps, the present local-density calculation underestimates them severely. With the exception of Ref. 15, the order of the gaps at Γ is identical to all calculations. The relative position of all conduction bands agree to within $\pm$0.3 eV. Note that the larger gaps obtained in the EPM calculations, while mandated in part by the fit to experiment, are also a consequence of omitting the Zn d orbitals from the model. The incorporation of the latter reduces the gaps.[24]

IV. ELECTRONIC CHARGE DENSITIES

The different valence subbands evident in Figs. 2—4 and in the generic band diagram in Fig. 5 are characterized by different distributions of the electronic charge density. This is depicted in Figs. 8—13.

The upper valence band (Figs. 8 and 9) can be characterized as representing a $A^{(II)}$—$C^{(V)}$ and $B^{(IV)}$—$C^{(V)}$ bonds, with a greater contribution to the former. The charge density is seen to be tetrahedrally distorted around the anion, with a sharper peak (shaded area) along the $A^{(II)}$—$C^{(V)}$ bond. At these energies, the cations bind mainly s waves and have nearly spherical charge contours near them. Whereas at the top of the upper valence band

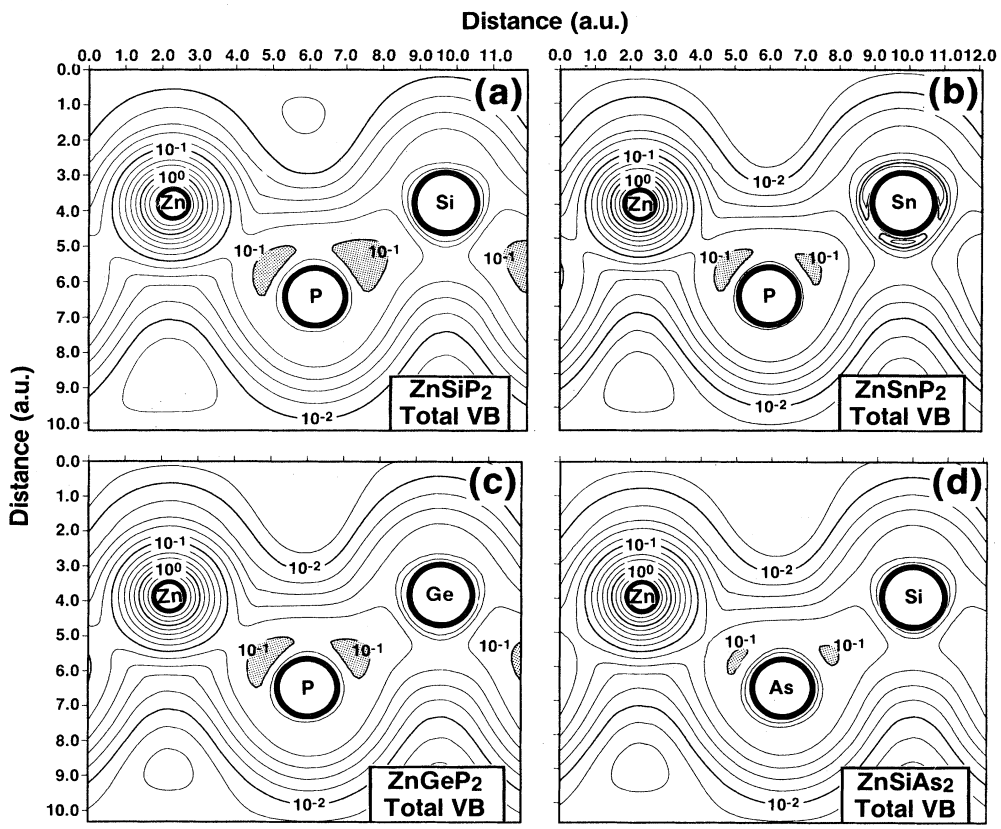

FIG. 14. Total valence charge density of (a) $ZnSiP_2$, (b) $ZnSnP_2$, (c) $ZnGeP_2$, and (d) $ZnSiAs_2$. The contours are logarithmically spaced; the solid circles denote the core regions. The 10^{-1}-e/a.u.^{3} contours on the bonds are shaded to highlight the maxima in the bond charges.

the majority of the charge lies along the $A^{(II)}$—$C^{(IV)}$ bond, as we approach the bottom of the upper valence band more charge becomes localized on the $B^{(IV)}$—$C^{(V)}$ bond.

At more negative energies we encounter the $B^{(IV)}$—$C^{(V)}$ bands that show a strong bond density on this contact (Figs. 10 and 11). In the Zn-based pnictides (Fig. 10), this band overlaps with the Zn $3d$ band that shows up as nearly spherical (i.e., d^{10}) charge-density contours in this energy region (Fig. 10). Since space near the Zn site is densely filled with the d electrons, the charge due to the $B^{(IV)}$-$C^{(V)}$ band is expelled from the Zn region and fills up to the $B^{(IV)}$—$C^{(V)}$ bond region. In the EPM calculations,[16] where the Zn $3d$ orbitals are absent, considerably more charge is spilled into the Zn—$C^{(V)}$ bond, rendering it artificially more stable (i.e., higher binding energies). Note that the radius of the Zn $3d$ charge density in Fig. 10 extends to almost half of the Zn—$C^{(V)}$ bond length, highlighting the non-frozen-core character of these orbitals. In $MgSiP_2$, lacking cation d orbitals, the charge density in the Si-P band approaches closer to the Mg site. The near resonance of the atomic energies of P and Si (recall that P forms a very shallow donor in Si, due to the close similarity in their atomic potentials and sizes) and the absence of an electron-repulsion effect from the $A^{(II)}$ cation, make the Si-P band unusually wide (Fig. 3) and places considerable density on this bond (Fig. 11).

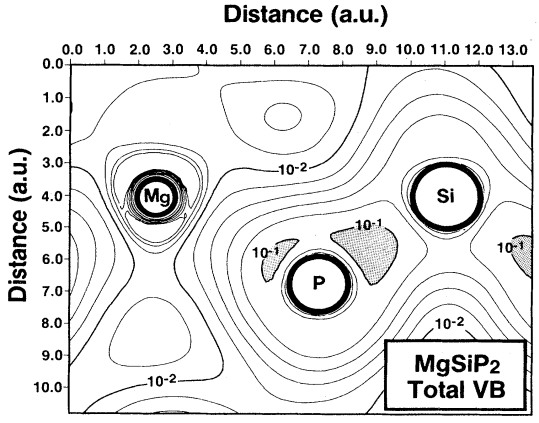

FIG. 15. Total valence charge density in $MgSiP_2$. The contours are logarithmically spaced; solid circles denote the core regions. The 10^{-1}-e/a.u.^{3} contours are shaded to highlight the maxima in the Mg—P and Si—P bond charges.

At still more negative energies, we encounter the $C^{(V)}$ s band, where the charge density (Fig. 12) is closely centered on the anion, with a tetrahedral deformation towards the $B^{(IV)}$ cation. Again, in $MgSiP_2$ this bond is more strongly polarized towards the $B^{(IV)}$ cation (Fig. 13), whereas in systems with a greater disparity between the anion and the $B^{(IV)}$-cation s-orbital energies (e.g., P and Sn in $ZnSnP_2$; Fig. 12), the overlap of these charge clouds is reduced.

The total valence-band charge (Figs. 14 and 15) clearly

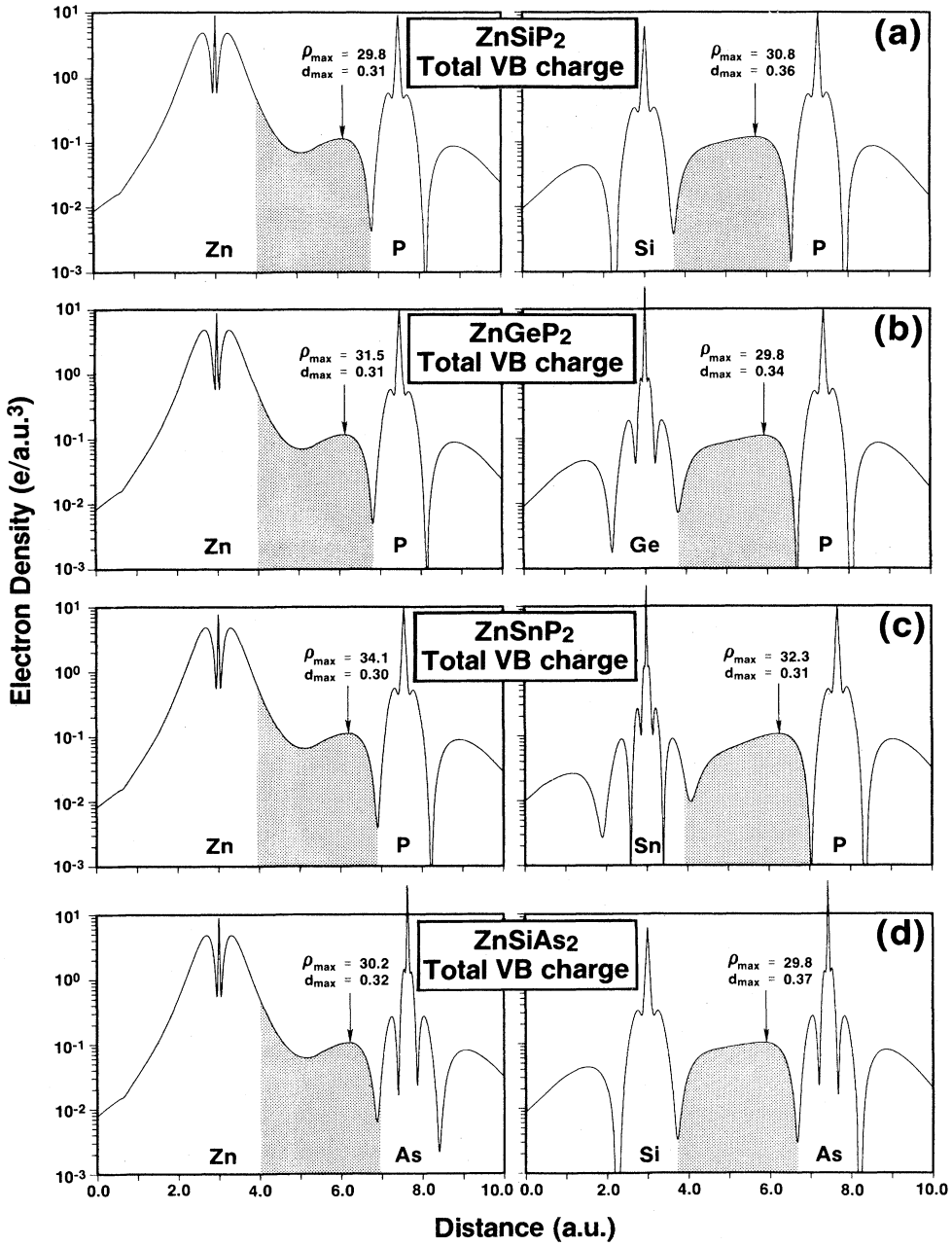

FIG. 16. Line plots of the valence charge density (in units of e/a.u.^{3}) along the $A^{(II)}$—$C^{(V)}$ and $B^{(IV)}$—$C^{(V)}$ bonds in ternary pnictides. The shaded areas denote the bond charge outside the core radii, taken as $\frac{1}{2}(r_s^\alpha + r_p^\alpha)$, where r_s and r_p are the density-functional orbital radii of Ref. 37. $d_{\max}$ denotes the distance from the anion, in units of the bond length R_{AC} or R_{BC}, at which the charge density reaches its maximum value $\rho_{\max}$. The latter is given in units of e/cell. (a) $ZnSiP_2$, (b) $ZnGeP_2$, (c) $ZnSnP_2$, and (d) $ZnSiAs_2$.

show the formation of two ($A^{(II)}$—$C^{(V)}$ and $B^{(IV)}$—$C^{(V)}$) cation—anion bonds, where their characteristics vary along this series. The chemical trends along the series of compounds considered here can be better appreciated by comparing the charge along bonds (Figs. 16 and 17). Here we have shaded the bond charge outside the core radii taken as $\frac{1}{2}(r_s^\alpha + r_p^\alpha)$, where r_s and r_p are the density-functional orbital radii and α denotes the atom type.[37] In each figure we give the value $\rho_{\max}$ of the highest charge density along the respective bond, together with the relative distance $d_{\max}$ of the peak density from the anion site, normalized to the respective anion—cation bond length. $d_{\max} = \frac{1}{2}$ indicates that the peak in the charge density is midway between the cation and the anion (i.e., "covalent" structure), whereas $d_{\max} \ll \frac{1}{2}$ suggests that the peak density is drawn towards the anion (i.e., "ionic" structure). Figures 16 and 17 show the $A^{(II)}$—$C^{(V)}$ bonds to be more ionic than the $B^{(IV)}$—$C^{(V)}$ bonds (i.e., smaller values of

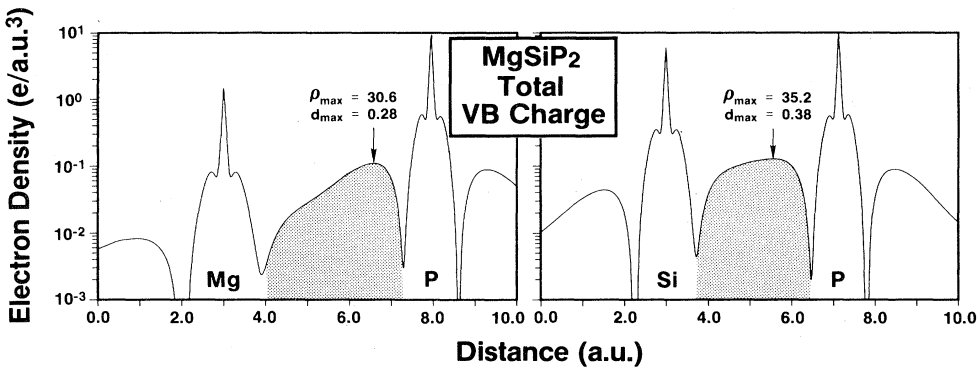

FIG. 17. Line plots of the valence charge density (in units of e/a.u.^{3}) along the Mg—P and Si—P bonds in $MgSiP_2$. The shaded areas denote the bond charge outside the core radii (cf. caption to Fig. 16).

d_{max} for the former bonds). When large and heavy atoms are involved (e.g., $ZnSnP_2$), the ionicity of the two bonds tends to equalize, forming a more metalliclike arrangement of charge. Conversely, when small atoms are involved (e.g., $MgSiP_2$ in Fig. 15), the disparity in bond ionicities increases. In EPM calculations,[21] involving a non-self-consistent charge distribution, the $B^{(IV)}$—$C^{(V)}$ bonds appear considerably more covalent (e.g., $d_{max} \simeq 0.47$ for the Ge—P bond in[21] $ZnGeP_2$, compared with $d_{max} = 0.34$ in the present study).

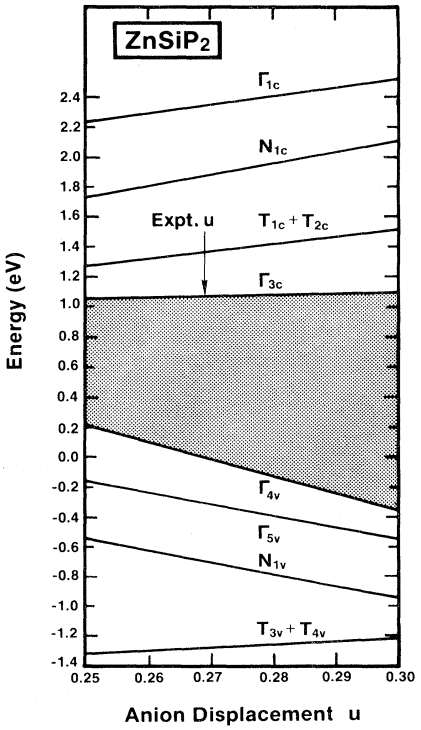

FIG. 18. Variation of the energies of some high-symmetry states in $ZnSiF_2$ with the anion displacement parameter u. The shaded area denotes the band gap. $u = \frac{1}{4}$ corresponds to the fictitious equal-bond structure ($R_{Zn-P} = R_{Si-P}$), whereas $u > \frac{1}{4}$ corresponds to the bond-alternating systems where the Zn—P bond expands and the Si—P bond shrinks as u increases.

From simple electrostatics[22,24] one expects that the $A^{(II)}$—$C^{(V)}$ bond will have less charge (and hence be longer) than the $B^{(IV)}$—$C^{(V)}$ bond, as the former represents a reduction from the average cation valency $\bar{Z} = (Z_A + Z_B)/2$ to $\bar{Z} - 1$, whereas the latter bond represents an increase from $\bar{Z}$ to $\bar{Z} + 1$. These point-ion electrostatic perturbations are screened by the valence electrons. Indeed, in the absence of $A^{(II)}$ d-electron effects ($MgSiP_2$ in Fig. 17), the $A^{(II)}$—$C^{(V)}$ bond contains less charge than the $B^{(IV)}$—$C^{(V)}$ bond (and has smaller ρ_{max} values). However, in the presence of d electrons (Fig. 16), the response of the valence electrons to the point-ion perturbations obscures the simple linear-response predictions, resulting either in a smaller ρ_{max} in the $A^{(II)}$—$C^{(V)}$ bond ($ZnSiP_2$, $ZnSiAs_2$), or in a larger one ($ZnSnP_2$). It is interesting to note that in the absence of $A^{(II)}$ d electrons (Fig. 15), both the $A^{(II)}$—$C^{(V)}$ and the $B^{(IV)}$—$C^{(V)}$ bond charges are confined to the bond region by two charge minima, one on each side of the bond center. On the other hand, when $A^{(II)}$ d orbitals exist (Fig. 16), only the $B^{(IV)}$—$C^{(V)}$ bond charge is similarly confined between two minima, whereas the $A^{(II)}$—$C^{(V)}$ bond charge is confined only on the anion side. This results in the strongest bond asymmetry in $MgSiP_2$, which is the most ionic member in this group. Turning to a fixed $A^{(II)}$ cation (Fig. 16), one notices that as the $B^{(IV)}$ atom changes down the column from Si to Ge and Sn, the asymmetry of the two anion—cation bonds reduces, suggesting a reduced covalency and increased metallicity. This trend is accompanied by an overall reduction in the band gaps (Table IV).

V. CALCULATED X-RAY-SCATTERING FACTORS

The calculated self-consistent electron charge density in the unit cell can be conveniently expressed in terms of its Fourier-series coefficients at the reciprocal-lattice vectors, which are equivalent to (suitably normalized) x-ray-scattering factors. Table VII shows the scattering factors for all five compounds for reciprocal-lattice vectors up to a fixed cutoff. The (0,0,0) scattering factors are defined to be equal to the number of electrons per unit cell. The scattering factors for $MgSiP_2$ are shown for two different values of anion displacements u to give an idea of their

TABLE VII. Calculated x-ray-scattering factors of $ZnSiP_2$, $ZnSnP_2$, and $MgSiP_2$ for the indicated values of the anion displacement parameters u. The scattering factors are in units of electrons per primitive unit cell. The reciprocal-lattice vectors are divided into three groups (Ref. 23), [(i)—(iii)]. Group (i) contains zinc-blende-like factors, group (ii) contains anion factors (vanishing for $u=\frac{1}{4}$), and group (iii) contains what is referred to as cation ionicity factors. See Ref. 23 for explicit definitions.

Reciprocal-lattice vectors	$ZnSiP_2$ $u=0.2691$	$ZnSiP_2$ $u=0.2500$	$ZnSnP_2$ $u=0.2390$	$MgSiP_2$ $u=0.3134$	$MgSiP_2$ $u=0.2848$
Group (i)					
(0,0,0)	148.00	148.00	220.00	112.00	112.00
(1,1,1)	85.31	85.49	145.53	58.41	60.29
(2,0,0)	26.85	26.22	89.33	0.80	3.76
(0,0,2)	26.15	26.16	89.14	4.80	4.78
(2,0,2)	95.68	96.16	155.48	63.28	67.01
(2,2,0)	95.87	96.90	155.32	59.54	67.25
(1,1,3)	64.37	64.48	115.87	42.26	43.57
(3,1,1)	64.65	65.23	115.78	37.86	43.11
(2,2,2)	23.10	22.18	75.68	6.91	0.93
(4,0,0)	79.97	81.72	131.66	43.81	54.37
(0,0,4)	80.21	80.21	132.25	56.25	56.38
(3,3,1)	55.98	56.97	100.76	29.47	36.58
(1,3,3)	55.89	56.44	100.84	32.58	37.27
(2,0,4)	17.95	17.55	64.66	0.51	2.44
(2,4,0)	20.14	18.06	65.23	16.49	3.37
(4,0,2)	19.58	17.93	65.08	11.72	1.82
(4,2,2)	70.33	72.31		34.50	46.96
Group (ii)					
(2,0,1)	0.57	0.00	0.17	6.21	1.92
(3,1,2)	0.87	0.00	0.30	8.87	2.91
(1,3,0)	0.97	0.00	0.31	9.81	3.24
(2,0,3)	0.40	0.00	0.15	4.68	1.43
(4,0,1)	1.68	0.00	0.58	15.86	5.54
(4,2,1)	1.23	0.00	0.42	10.79	3.96
Group (iii)					
$(1,0,\frac{1}{2})$	19.06	22.22	24.20	12.73	8.14
$(3,0,\frac{3}{2})$	11.14	16.96	16.54	16.83	11.48
$(2,1,\frac{3}{2})$	17.12	18.82	20.48	15.83	9.44
$(4,1,\frac{5}{2})$	15.80	12.70	18.84	14.90	11.15
$(4,1,\frac{3}{2})$	17.10	13.92	19.60	15.65	11.64
$(2,1,\frac{1}{2})$	22.89	19.98	24.22	16.11	9.23
$(3,2,\frac{5}{2})$	19.26	13.73	21.38	16.32	9.84
$(3,2,\frac{1}{2})$	11.18	16.19	16.20	20.36	13.24
$(3,0,\frac{1}{2})$	24.07	17.88	24.46	15.38	9.63
$(3,0,\frac{5}{2})$	9.74	15.26	15.58	16.05	10.92
$(1,0,\frac{3}{2})$	23.82	21.17	25.45	7.00	3.24
$(3,2,\frac{3}{2})$	21.17	15.28	22.39	17.46	10.57
$(1,4,\frac{1}{2})$	14.65	14.67	17.91	17.16	12.80
$(1,2,\frac{5}{2})$	15.45	16.89	19.00	13.93	8.37
$(3,0,\frac{7}{2})$	18.20	13.14	20.79	11.71	7.11
$(1,0,\frac{5}{2})$	20.82	18.60	22.99	5.75	2.60

TABLE VII. (*Continued*).

Reciprocal-lattice vectors	$ZnSiP_2$ $u=0.2691$	$ZnSiP_2$ $u=0.2500$	$ZnSnP_2$ $u=0.2390$	$MgSiP_2$ $u=0.3134$	$MgSiP_2$ $u=0.2848$
$(1,2,\frac{7}{2})$	16.50	14.33	19.71	11.41	6.44
$(1,0,\frac{7}{2})$	13.96	15.81	18.31	7.37	4.73
$(1,0,\frac{9}{2})$	11.33	13.03	16.67		

TABLE VIII. Calculated x-ray-scattering factors for $ZnGeP_2$ and $ZnSiAs_2$, compared with the experimental data of Lind and Grant (Ref. 31) (divided by 2 to normalize the same unit-cell volume). [The notation (n,l,m) of Ref. 31 corresponds to our notation $(n,l,m/2)$.]

	$ZnGeP_2$ ($u=0.258\,16$)		$ZnSiAs_2$ ($u=0.265\,75$)	
$\vec{G}$	$\rho_{calc}(\vec{G})$	$\rho_{expt}(\vec{G})$	$\rho_{calc}(\vec{G})$	$\rho_{expt}(\vec{G})$
Group (i)				
(0,0,0)	184.00	184.00	220.00	220.00
(2,0,0)	58.64	55.80	37.20	26.55
(0,0,2)	58.36	57.50	37.94	28.10
(2,0,2)	126.00	124.10	155.78	158.55
(1,1,3)	89.59	89.40	104.85	101.20
(3,1,1)	90.15	87.95	104.41	106.85
(2,2,2)	49.22	47.00	30.11	29.50
(2,0,4)	40.74	37.65	27.84	26.30
(2,4,0)	41.61	37.80	25.13	25.00
(4,0,2)	41.39	37.90	25.82	24.65
(4,2,2)	93.95	86.10	115.08	104.90
Group (ii)				
(2,0,1)	0.07	<1.35	0.99	<2.15
(3,1,2)	0.14	<2.20	1.61	<2.75
(1,3,0)	0.15	<2.75	1.76	<4.95
(2,0,3)	0.04	<1.95	0.78	<2.95
(4,0,1)	0.29	<2.00	3.09	3.00
(4,2,1)	0.22	<1.85	2.21	<2.75
Group (iii)				
$(1,0,\frac{1}{2})$	3.63	4.25	16.20	16.55
$(2,1,\frac{3}{2})$	3.53	3.90	17.13	16.50
$(4,1,\frac{5}{2})$	3.39	3.50	22.01	18.70
$(4,1,\frac{3}{2})$	3.35	4.20	23.59	21.20
$(2,1,\frac{1}{2})$	2.38	2.55	27.28	27.25
$(3,2,\frac{5}{2})$	1.63	<2.00	26.71	23.15
$(3,2,\frac{1}{2})$	4.88	5.70	9.32	8.95
$(3,0,\frac{1}{2})$	0.59	<1.30	31.83	30.80
$(3,0,\frac{5}{2})$	4.57	5.40	3.54	4.20
$(1,0,\frac{3}{2})$	0.79	<1.40	26.76	26.20
$(3,2,\frac{3}{2})$	1.42	2.40	29.00	25.90
$(1,4,\frac{1}{2})$	4.32	5.55	19.08	18.15
$(1,2,\frac{5}{2})$	3.30	4.35	15.57	14.85
$(1,0,\frac{5}{2})$	1.20	2.30	23.70	22.65
$(1,2,\frac{7}{2})$	2.09	3.40	20.25	17.50

dependence on that parameter. In Table VIII we compare our calculated scattering factors with those measured by Lind and Grant.[31] Our calculated scattering factors are seen to be larger in every case, but it must be recalled that our calculation applies to zero temperature, while the experimental factors are reduced by the effects of finite temperature (primarily by Debye-Waller factors). Unfortunately, there is no feasible exact method for including the effects of temperature in our calculated structure factors; an approximate method used by us before[23] gave somewhat improved agreement in the present case. It is interesting to note that whereas the scattering factors that belong to group (i) (i.e., already allowed in the zinc-blende lattice) are large, the non-zinc-blende factors of group (iii) are often comparable in size, reflecting the formation of new anisotropic components of a chalcopyrite-specific bond charge. On the other hand, group-(ii) scattering factors directly reflect the anisotropy associated with a distorted anion sublattice and are uniformly small. We next turn to the effect of this anion displacement on the band structure.

VI. ANION DISPLACEMENT EFFECTS

We have previously[24–26] analyzed in detail the effect of bond alternation (i.e., $R_{AC} \neq R_{BC}$ in ABC_2 systems) on the one-particle spectra of I-III-VI_2 chalcopyrites[24,25] and on III-III-V_2 pseudochalcopyrites.[26] We have shown that both the band-gap anomaly in the former group (i.e., band gaps are smaller than in the analogous binary II-VI semiconductors), and the optical bowing in the latter group (i.e., band gaps of alloys of III-V semiconductors are smaller than the concentration-average gap of the constituent pure semiconductors) share in common the same physical origin, i.e., bond alternation. Here, we indicate that the II-IV-V_2 pnictides are no exception. Figure 18 shows the variation of some of the high-symmetry band states in $ZnSiP_2$ with the anion displacement parameter u, as obtained from a series of self-consistent calculations with different u values. In the hypothetical structure with $u = \frac{1}{4}$, both bond lengths R_{Zn-P} and R_{Si-P} are equal. The observed u value of 0.27 corresponds to the situation where $R_{Zn-P} > R_{Si-P}$, that is,[24] where the Zn—P and Si—P bonds attain their canonical values in a tetrahedral environment. Figure 18 shows that as the bonds start to alternate (u increases from $u = \frac{1}{4}$), the occupied valence bands are stabilized, moving down in energy, and the antibonding conduction bands are destabilized, moving up in energy. As in the ternary I-III-VI_2 chalcopyrites, the band gap is hence partially controlled by the anion displacement. The different ABC_2 systems can be classified, in this respect, in terms of the sensitivity of their band gaps to bond alternation. We find that for the systems with the largest disparity between the sizes and electronegativities of the A and B cations (i.e., I-III-VI_2 chalcopyrites) the gap derivative $\partial E_g/\partial u$ is the largest (18—21 eV), decreasing for the ternary pnictides to 11—12 eV, and finally, for the III-III-V_2 pseudochalcopyrites (e.g., $InGaP_2$), the gap derivative ranges between 1 and 3 eV. (In the empirical pseudopotential calculation of Ref. 22, a considerably higher value of 18.7 eV is obtained for $ZnGeAs_2$. However, in the EPM calculation of Ref. 18, the calculated gap derivative for $ZnSiP_2$ was 6.8 eV.)

We have previously discussed the change in the charge distribution attending bond alternation in ABC_2 chalcopyrites.[24–26] Since the results for the ternary pnictides are qualitatively similar, we will only summarize the results for $ZnSiP_2$. We find that as we go from the equal-bond structure ($u = \frac{1}{4}$) to the bond-alternating structure ($u > \frac{1}{4}$), excess charge is placed on the bond that is shortened (Si—P in $ZnSiP_2$, or Cu—Se in $CuInSe_2$) near its maximum, and charge is depleted from the bond that is elongated (Zn—P in $ZnSiP_2$ or In—Se in $CuInSe_2$), near its maximum. This trend stabilizes the states whose wave functions have a larger amplitude on the bond that gets shortened (i.e., the top of the upper valence band that contains a majority Si-P character in $ZnSiP_2$, or a majority Cu-Se character in $CuInSe_2$). This trend also destabilizes the states whose wave functions have a larger amplitude on the bonds that are elongated (i.e., the conduction band that has a majority Zn-P character in $ZnSiP_2$, or In-Se character in $CuInSe_2$). In the recent local pseudopotential calculation[22] on $ZnGeAs_2$ it was found that in going from $u = \frac{1}{4}$ to $u > \frac{1}{4}$ (keeping η fixed, as we do), more charge was placed on the expanding Zn—As bond (near its maximum) and charge was slightly depleted from the shrinking Ge—As bond. Our results contradict this finding. A trend consistent with our results was observed by Serra *et al.*[38] in their empirical pseudopotential calculation on $CdGeP_2$, where upon going from $u = \frac{1}{4}$ to $u > \frac{1}{4}$, more charge was placed on the shrinking bond (P—Ge), whereas charge was depleted from the expanding bond (Cd—P).

ACKNOWLEDGMENTS

This work was supported in part by the Division of Materials Science, Office of Energy Research, U.S. Department of Energy, under Grant No. DE-AC02-77-CH00178.

*Present address: Department of Physics, State University of New York, Stony Brook, NY 11794.

[1]J. L. Shay and J. H. Wernick, *Ternary Chalcopyrite Semiconductors: Growth, Electronic Properties and Applications* (Pergamon, Oxford, 1974).

[2]B. R. Pamplin, T. Kiyosawa, and K. Masumoto, Prog. Cryst. Growth Charact. 1, 331 (1979).

[3]R. A. Mickelsen and W. S. Chen, in *Proceedings of the Fifteenth IEEE Photovoltaic Specialists Conference, 1981* (IEEE, New York, 1981), p. 800, available as IEEE Publ. 81CH1644-4.

[4]G. D. Boyd, E. Buehler, and F. G. Storz, Appl. Phys. Lett. 18, 301 (1971).

[5]G. F. Karavaev, A. S. Poplavnoi, and V. A. Chaldyshev, Fiz. Tekh. Poluprovdn. 2, 113 (1968) [Sov. Phys.-Semicond. 2, 93 (1968)].

[6]A. S. Poplavnoi, Yu. I. Polygalov, and V. Chaldyshev, Izv. Vyssh. Ucheb. Zav. Fiz. **12**, 58 (1969) [Sov. Phys. J **12**, 1415 (1969)].
[7]A. S. Poplavnoi, Yu. I. Polygalov, and V. Chaldyshev, Izv. Vyssh. Ucheb. Zav. Fis. **13**, 17 (1970); **13**, 95 (1970) [Sov. Phys. J. **13**, 766 (1970); **13**, 849 (1970)].
[8]N. A. Goryunova, A. S. Poplavnoi, Yu. I. Polygalov, and V. A. Chaldyshev, Phys. Status Solidi **39**, 9 (1970).
[9]Yu. J. Polygalov, A. S. Poplavoni, and A. M. Ratner, J. Phys. (Paris) Colloq. **36**, C3-129 (1975).
[10]A. Shileika, Surf. Sci. **37**, 730 (1973).
[11]R. Bendorius, V. D. Prochukhan, and A. Shilekia, Phys. Status Solidi B **53**, 745 (1972).
[12]D. J. Morgan, Phys. Status Solidi B **48**, 771 (1971).
[13]A. M. Altshuler, Yu. Kh. Vekilov, and G. R. Umarov, Phys. Status Solidi B **90**, 733 (1978).
[14]C. V. de Alvarez and M. L. Cohen, Phys. Rev. Lett. **30**, 979 (1973).
[15]C. V. de Alvarez, M. L. Cohen, S. E. Kohn, Y. Petroff, and Y. R. Shen, Phys. Rev. B **10**, 5175 (1974).
[16]C. V. de Alvarez, M. L. Cohen, L. Ley, S. P. Kowalczyk, F. R. McFeely, D. A. Shirley, and R. W. Grant, Phys. Rev. B **10**, 596 (1974).
[17]J. F. Alward and C. Y. Fong, Phys. Rev. B **19**, 6338 (1979).
[18]L. Pasemann, W. Cordts, A. Heinrich, and J. Monecke, Phys. Status Solidi B **77**, 527 (1976); B **96**, 201 (1979).
[19]A. Heinrich, W. Cordts, and J. Monecke, Phys. Status Solidi B **107**, 319 (1981).
[20]L. Pasemanm, Phys. Status Solidi B **56**, K69 (1973).
[21]F. Aymerich, G. Mula, A. Balderschi, and F. Meloni, in *Ternary Compounds,* edited by G. D. Holah (Institute of Physics, Bristol, 1977), p. 159.
[22]A. Balderschi, F. Meloni, and M. Serra, Il. Nuovo Cimento D **2**, 1643 (1983).
[23]J. E. Jaffe and A. Zunger, Phys. Rev. B **28**, 5822 (1983). This paper contains references to previous papers on band structures of I-III-VI_2 compounds.
[24]J. E. Jaffe and A. Zunger, Phys. Rev. B **29**, 1882 (1984).
[25]J. E. Jaffe and A. Zunger, Phys. Rev. B **27**, 5176 (1983).
[26]A. Zunger and J. E. Jaffe, Phys. Rev. Lett. **51**, 662 (1983).
[27]P. Bendt and A. Zunger, Phys. Rev. B **26**, 3114 (1982).
[28]D. M. Ceperley and B. J. Alder, Phys. Rev. Lett. **45**, 566 (1980); D. M. Ceperley, Phys. Rev. B **18**, 3126 (1978).
[29]D. M. Wood and A. Zunger (unpublished).
[30]S. C. Abrahams and J. L. Bernstein, J. Chem. Phys. **52**, 5607 (1970).
[31]M. D. Lind and R. W. Grant, J. Chem. Phys. **58**, 357 (1973).
[32]A. A. Vaipolin, N. A. Goryunova, L. I. Keshchinskii, G. V. Loshakova, and E. D. Osmanov, Phys. Status Solidi **29**, 435 (1968).
[33]A. A. Vaipolin, Fiz. Tverd. Tela **15**, 1430 (1973) [Sov. Phys.—Solid State **15**, 965 (1973)].
[34]A. Zunger, J. Vac. Sci. Technol. **16**, 1337 (1979); J. P. Perdew and A. Zunger, Phys. Rev. B **23**, 5048 (1981).
[35]*Ternary Chalcopyrite Semiconductors: Growth, Electron Properties and Applications,* Ref. 1, p. 82.
[36]J. L. Shay, B. Tell, E. Buehler, and J. H. Wernick, Phys. Rev. Lett. **30**, 983 (1973).
[37]A. Zunger, Phys. Rev. B **22**, 5839 (1980).
[38]M. Serra, F. Aymerich, F. Meloni, and G. G. Pegna, Solid State Commun. **49**, 119 (1964).